Published in final edited form as:

Scanning. 2014 ; 36(2): 231–240. doi:10.1002/sca.21093.

Crystallographic Texture and Elemental Composition Mapped in Bovine Root Dentin at the 200 nm Level

A. C. Deymier-Black[1], **A. Veis**[2], **Z. Cai**[3], and **S. R. Stock**[4]

[1]Department of Materials Science and Engineering, Northwestern University, Evanston, Illinois

[2]Department of Cell and Molecular Biology, Northwestern University, Chicago, Illinois

[3]Advanced Photon Source, Argonne National Laboratory, Argonne, Illinois

[4]Department of Molecular Pharmacology and Biological Chemistry, Northwestern University, Chicago, Illinois

Summary

The relationship between the mineralization of peritubular dentin (PTD) and intertubular dentin (ITD) is not well understood. Tubules are quite small, diameter ~2 μm, and this makes the near-tubule region of dentin difficult to study. Here, advanced characterization techniques are applied in a novel way to examine what organic or nanostructural signatures may indicate the end of ITD or the beginning of PTD mineralization. X-ray fluorescence intensity (Ca, P, and Zn) and X-ray diffraction patterns from carbonated apatite (cAp) were mapped around dentintubules at resolutions ten times smaller than the feature size (200 nm pixels), representing a 36% increase in resolution over earlier work. In the near tubule volumes of near-pulp, root dentin, Zn intensity was higher than in ITD remote from the tubules. This increase in Zn^{2+}, as determined by X-ray absorption near edge structure analysis, may indicate the presence of metalloenzymes or transcription factors important to ITD or PTD mineralization. The profiles of the cAp 00.2 X-ray diffraction rings were fitted with a pseudo-Voigt function, and the spatial and azimuthal distribution of these rings' integrated intensities indicated that the cAp platelets were arranged with their *c*-axes aligned tangential to the edge of the tubule lumen. This texture was continuous throughout the dentin indicating a lack of structural difference between in the Zn rich near-tubular region and the remote ITD.

Keywords

dentin; tubule; X-ray diffraction mapping; X-ray fluorescence mapping; zinc

Address for reprints: S. R. Stock, Department of Molecular Pharmacology and Biological Chemistry, Northwestern University, Chicago, IL 60611-3008. s-stock@northwestern.edu.

A. C. Deymier-Black's current address: Department of Orthopaedic Surgery, Washington University in St. Louis, St. Louis, MO 63130.

Introduction

Dentin, the main component by volume of mammalian teeth, is a porous mineralized tissue which provides toughness to the dental organ. On the microscopic level, a defining feature of dentin is the tubules running from near the dentinoenamel junction (DEJ) to the pulp cavity. These long channels are produced by odontoblasts moving away from the DEJ during growth and are filled with odontoblastic processes or their remnants, that is, fluid or soft tissue. The dentin surrounding these tubules contains two phases: intertubular dentin (ITD), which forms between the odontoblastic processes (tubules), and peritubular dentin (PTD), which grows after ITD mineralizes and around the circumference of the tubule and into its lumen. ITD makes up most of the volume of dentin and is a composite consisting of a matrix of collagen fibrils discontinuously reinforced with nano-platelets of carbonated hydroxyapatite (cAp) making it strong but tough (Ten Cate, ’80). PTD forms as relatively thin collars at the margins of the 1–2 μm diameter tubules in species such as *Homo sapiens* and *Bostaurus*. PTD is more highly mineralized than ITD (Takuma and Eda, ’96; Weber, ’68; Weiner *et al*., ’99) but contains little to no collagen (Weiner *et al*., ’99; Gotliv *et al*., 2006; Gotliv and Veis, 2007) making it significantly harder and stiffer than the ITD (Kinney *et al*., ’96). The thickness and distribution of PTD is highly variable and depends in part on the age and location of the dentin (Takuma and Eda, ’96; Weber, ’68). It remains unclear exactly how cAp in ITD and in PTD are related to each other and how PTD forms adjacent to ITD.

In bovine apical root dentin near the pulp cavity or in very early stages of development, PTD is often absent (Takuma and Eda, ’96). Studying tubules in near-pulp root dentin, therefore, provides a baseline structure against which PTD-containing tubules can be compared and should lead to identification of organic species or nanostructures related to the initiation and growth of PTD. Recently, nanoscale (250 nm) synchrotron fluorescence and diffraction mapping of bovine dentin (Stock *et al*., 2011) at the Advanced Photon Source (APS, Argonne National Laboratory) found Zn concentrated near the tubules. This is interesting as Zn is often found to be present at mineralizing fronts in biological tissues (Vincent, ’63; Gomez *et al*., ’99; Zoeger *et al*., 2008). Second, rather primitive analysis of the diffraction patterns found that the cAp *c*-axes, which lie parallel to the fibril axes, lie more-or-less perpendicular to the axis of the tubule they surround. This arrangement of crystal axes around the tubule lumen is a type of biaxial crystallographic texture that produces characteristic variation of diffracted intensity with position. The results of Stock *et al*. (2011) suggest that improved data collection and analysis would provide valuable insight into the ITD-PTD system.

In the present study, synchrotron fluorescence and diffraction mapping techniques were improved from Stock *et al*. (2011), producing a 36% increase in sampling volume resolution (beam cross-section decreased from 250 × 250 nm^2 to 200 × 200 nm^2), a significantly more accurate analysis of the diffraction data and improved statistics in the fluorescence analysis. X-ray fluorescence maps of thirteen tubules confirmed the presence of Zn in the near-tubular dentin. The increased resolution facilitated more accurate determinations of Zn distributions about these tubules. Additionally, X-ray absorption near-edge structure (XANES) was used to investigate zinc’s valence state. In order to analyze cAp crystallographic texture, the weak

diffraction rings were fitted and the azimuthal variation of intensity with position was mapped within six sectors, an approach considerably superior to the crude detector regions-of-interest used in Stock *et al*. (2011). The fitting routines not only improved texture analysis but also allowed the data to be examined for the presence of residual strains and of strain distributions (root-mean-square strain) in the cAp nanoplatelets. Within the context of these findings, the role of Zn content and near-tubular dentin texture on possible PTD mineralization is discussed.

Materials and Methods

Sample Preparation

An erupted bovine molar was extracted from an animal 12–18 months in age and cast in LR white (Electron Microscopy Sciences, Hatfield, PA). Cuts were made perpendicular to the molar's occlusal-apical axis using an Isomet 1,000 wafering saw (Buehler, Lake Bluff, IL) at intervals of 2.0 mm. The resulting slabs were numbered from crown to root. The specimens used in this study were taken from slab 7, which is located in the root dentin approximately 2–4 mm below the cervical line. Slab7 was cut into rectangular blocks spanning the cementum to the pulp. These blocks had a cross-section of 1.7 mm × 1.3 mm with the larger dimension being along the crown-root axis. One block from slab 7 was prepared for microtome sectioning by casting it in a small mold filled with LR white.

The mounted block was then sectioned into ~1 μm thick slices using an Ultramicrotome UC6 (Leica Microsystems, Bannockburn, IL) with aDiAtome Diamond Histoknife (EMS, Hatfield, PA). The block was cut from the side nearest the pulp so that the thin sections were located no closer than 50 μm and no farther than 200 μm from the mineralization front. The tubule axes were approximately perpendicular to the plane of the thin sections. The thin sections in water droplets were deposited onto small squares of polyimidepolymer (kapton, 12.5 μm thickness, DuPont, Circleville, OH). The water was then allowed to evaporate, depositing the thin section securely onto the kapton. One slice was mounted directly on an amorphous silicon-nitride window (Silson, Blisworth, Northampton, UK).

X-Ray Examination

The thin sections were examined at station 2-ID-D, APS, using the X-ray microprobe described elsewhere (Libera *et al*., 2002). The dentin thin sections were placed normal to the incident X-ray beam at the focal plane of the X-ray zone plate and at the rotation center of the diffractometer as shown in Figure 1. The samples were examined using an X-ray beam with a 200 × 200 nm cross-section and a 10.1 keV energy. Both X-ray fluorescence and diffraction measurements were performed simultaneously on all of the samples.

The fluorescence intensities were mapped using a Vortex-EX silicon drift detector (SII Nanotechnology USA, Northridge, CA) positioned as close as possible to the specimen and aligned to collect X-rays emerging nearly parallel to the front surface of the specimen and in the horizontal plane (i.e., the plane of the storage ring) for the best signal-to-noise ratio. Windows were set in the multichannel analyzer at energies spanning the following K lines: Ca, P, and Zn. The Ca peak had the highest intensity, and P and Zn signals were also

significantly above background. The air path was too long for detection of the Na and Mg peaks.

Wide-angle X-ray scattering (diffraction) peaks from cAp were mapped with a QUAD-RO CCD detector (Princeton Instruments, Trenton, NJ) placed behind the specimen. The detector was placed at a sample-to-detector distance of 34.2 mm normal to the transmitted beam and centered on it. At this sample-to-detector distance, the 00.2[1] and unresolved 21.1 + 11.2 + 30.0 cAp diffraction rings (20.4 and 25.0–25.9° 2θ, respectively) were recorded in their entirety.

The samples were positioned in the X-ray beam by observing radiographs of the specimen produced by the unfocused beam after moving the order sorting aperture out of the beam. The radiographic contrast was poor, but large features could be observed from strong phase contrast at the borders of tears, folds and the sample. Using these features as references, the sample was then translated to areas where there were no folds or tears, where the tubules were nearly perpendicular to the section plane and where the tubules were not too tightly clustered.

Rapid scans over larger areas of 25 × 25 μm^2 identified individual tubules for mapping (400 nm translation steps, acquisition of only Ca fluorescent signal, 1 s/position, ~1.5 hr duration). After selecting specific tubules, six high resolution scans were recorded (200 nm steps, 40 or 50 s/position integration for fluorescence, 60 s/position integration for the diffraction pattern) covering one or two tubules, spanning areas of 5.2–6.6 μm across. At 60 s/position, covering a $(6\ \mu m)^2$ area required approximately 16 hr. In order to characterize more tubules in the limited beam time available, two perpendicular line scans were recorded across the center of each of seven additional tubules. These scans were 6.2–8.2 μm in length (200 nm steps, 50 s integration for fluorescence, 60 s/position integration for the diffraction pattern).

Fluorescence Analysis

To account for variations in X-ray beam intensity, fluorescence intensities were normalized using the incoming beam intensity measured by an ionization detector placed before the specimen. The normalized Ca and Zn fluorescence intensities were plotted as a function of position for all of the mapped samples as shown in Figure 2. The tubule lumens were easily discerned in these fluorescence maps by their low Ca and Zn signals. The position of the lumen edge was defined as the location where the Ca fluorescence was less than 40% of the peak Ca intensity in the sample map.

Diffraction Analysis

Analysis of the diffraction data was performed as described elsewhere (Almer and Stock, 2005; Singhal *et al*., 2011) and is summarized here. This approach had not been previously applied to the dentin thin sections studied with beam dimensions less than one micrometer. Using the identified cAp 00.2 diffraction peak, the fitting program Fit2D (Hammersley, ’98)

[1]Note the use of Miller Bravais indices for this hexagonal crystal system.

refined a number of parameters including sample-to-detector distance, detector tilt, and detector rotation. The shapes of the cAp 00.2 and cAp 21.1 + 11.2 + 30.0 diffraction peaks were fitted using a pseudo-Voigt type curve after subtracting background.[2] To increase statistics for these very low intensity peaks, the fit was performed over 15° azimuthal bins starting between 0° and 15° and continuing around the pattern (see Figure 1 for the definition of the azimuthal angles). From these fits, the integrated intensities, measured from the area under the fitted curve, were determined for particles with their *c*-axes aligned at angles of 0°, 30°, 60°, 90°, 120°, and 150° ± 15°. The integrated intensity of an angle of interest is calculated by taking the average of the integrated intensity of the bins on either side of the angle of interest as well as the bins adjacent to the complementary angle of interest (i.e., 0 ± 15° Combined with 180 ± 15°). Like the fluorescence intensity values, the integrated diffracted intensities were normalized by the incident X-ray beam intensity to account for beam intensity variations. For the diffraction maps, the integrated intensities for each range of angles were plotted as a function of position as shown in Figure 2.

The radial position of the 00.2 diffraction ring, *R*, was determined from the location of the center of the pseudo-Voigt fitted peak. These radial positions were then converted to *d*-spacing using Bragg's law: $\lambda = 2\, d_{\mathrm{hkl}} \sin\theta$, where λ is the X-ray wavelength, d_{hkl} is the Bragg spacing of the *hkl* reflection and θ is the diffraction angle which is equal to $(1/2)\tan^{-1}(R/z)$ with *z* being the sample to detector distance. With the measured reference and local *d*-spacings, d_0 and d_1, respectively, the longitudinal residual strains in the dentin were then calculated from the definition of strain, $\varepsilon_1 = (d_1 - d_0)/d_0$, and the apparent cAp Poisson's ratio measured in dentin of $\nu_{21} = 0.22$ (Deymier-Black *et al*., 2010). The reference position is taken at a point in the ITD far from the tubule lumens.

The full width half maximum (FWHM) of the 00.2 diffraction ring was measured as the average of the FWHM of the pseudo-Voigt fitted peak for each 15° bin. From this FWHM and assuming an average longitudinal platelet size of 50 nm (Deymier-Black *et al*., 2012), the root mean square (RMS) strain, that is, the distribution of cAp strain in the sampled volume, is:

$$\Delta 2\theta \cos\theta = 2\varepsilon_{\mathrm{rms}} \sin\theta - \frac{\lambda}{t}$$

where $\Delta 2\theta$ is the FWHM of the 00.2 peak in radians, *t* is the platelet size, and $\varepsilon_{\mathrm{rms}}$ is the RMS strain.

XANES (X-Ray Absorption Near Edge Structure)

X-ray absorption near edge structure was recorded from a dentin specimen and two standards using the same beam dimensions as in the mapping experiments. The dentin thin section XANES was obtained at a position near a tubule identified as having high Zn content in earlier mapping. One standard was a Zn metal foil, and the second a powder of zinc gluconate hydrate (CAS 4468-02-4) containing Zn^{2+}. The monochromator was scanned over

[2]Hereafter the unresolved cAp 21.1 + 11.2 + 30.0 diffraction peak is abbreviated as 21.1+.

the energy range encompassing the Zn K-edge: 9.626–9.726 keV in 1 eV steps. The counting time was 15 s per energy step, and intensity of the Zn Kα fluorescent line was measured.

Results

Fluorescence

Fluorescence maps with 200 nm pixels were obtained for six areas taken from four different microtomed bovine dentin slices. Fluorescence line scans were recorded for seven additional tubules from three of the four dentin slices used for area mapping. Figure 2A shows a single tubule from one slice, and Figure 2B shows two neighboring tubules in a second. These maps are representative of the other maps not shown. In the area shown in Figure 2A, the maximum counts for P, Ca, and Zn were 2.6×10^3, 7.44×10^4, and 4.0×10^3, respectively, and, in Figure 2B, 2.8×10^3, 7.79×10^4, and 4.7×10^3, respectively. For comparison, the Zn counts within the tubule lumens were about one-third of those at the peak positions in the dentin and one-half those in the ITD remote from the tubule. The ratio of Ca within the lumen to that in the ITD was somewhat lower than that for Zn.

Zn signal was highest in the dentin in the vicinity of the tubule lumens, was irregularly distributed around the circumference of the lumens, and was often higher on one side of the tubule than the other (Fig. 2). The one-dimensional scans across tubules also showed asymmetric Zn fluorescence intensity (Fig. 4, as well as other scans not shown). Ignoring the asymmetrical Zn distribution and averaging around successive one pixel wide shells moving out from the lumen edge, produces the plots shown in Figure 3B. In order to aid comparison of the different scans, the intensity of each plot of Figure 3 was scaled to 1.0 at the lumen edge for both Ca and for Zn. There were sizeable numerical variations in width and shape of the Zn intensity profiles within the six circumferentially averaged area maps of Figure 3B. In most cases, the Zn fluorescence intensity reached a maximum ~0.4 μm from the lumen edge, but sometimes the peak was as far as 0.8 μm from the lumen edge. After this peak, the Zn intensity decreased until it reached a plateau approximately 1.0–1.2 μm from the lumen edge. From circumferential averages of Zn intensity about the tubules shown in Figure 3B, the maximum of the Zn peak ranged from 6% to 28% higher than the Zn intensity at the lumens' edges and averaged about 12% higher. The maximum Zn intensity averaged 29 ± 13% above the Zn intensity at the lumen edge for the six maps. The scatter bars in Figure 3 are standard deviations of the intensity values measured about the tubule in each 1 pixel shell; therefore, larger bars represent greater inhomogeneity in the Zn fluorescence intensity about the tubule circumference. In the line scans, the Zn peak intensity was as low as 2% and as high as 34% (mean of 11%) above the intensity far from the tubule (mean of the three points in the scan farthest from the tubule); these individual plots are not shown, only the average of the line scans. Nearly all of the Zn intensity above background (95%) is located within a distance of 0.8 and 2.4 μm from the lumen edge.

In the two maps of Figure 2 and all other samples examined (both area maps and line scans), Ca fluorescence increased rapidly and relatively homogeneously adjacent to the lumen edge and then plateaued ~1.2 μm from the lumen edge (Fig. 3A). The P/Ca fluorescent intensity ratio is constant between samples, with a mean value of 0.035 ± 0.003. Note that this

average and all other averages computed from the area maps and line scans exclude those pixels inside the tubule lumen (i.e., those pixels whose Ca fluorescence was less than 40% of the peak Ca intensity in that map). The P/Ca ratio is somewhat lower near the tubules than in the remote ITD (Figure 2).

In both maps of Figure 2, the tubules had an elongated non-circular shape. The average diameter of the tubules was determined from the Ca line scans as well from vertical and horizontal profiles across the mapped tubules. The distance between the lumen edges defined the tubule diameter and averaged 1.7 ± 0.5 μm.[3]

Diffraction

For all of the samples used in this study, the diffraction patterns revealed only the cAp 00.2 and the unresolved 21.1+ peaks. These peaks were quite weak, for example, 550 cts in a single pixel of the 00.2 ring compared to 500 cts in a background pixel. For the position with maximum intensity in the map in Figure 2A, the integrated intensity of an entire 00.2 ring was 318 cts above background.

The intensity of the 00.2 peak varied with azimuthal angle but that of the 21.1+ peak did not. The top six maps of Figure 2A,B plot, as a function of position, the intensity of the 00.2 cAp diffraction peak over a specific azimuthal range of angles (the angle shown in each map ±15°). This pattern of diffracted intensities was representative of the other four maps not shown. These maps indicated that nanoplatelets with their *c*-axes preferentially aligned along the 0° azimuth were mainly located above or below the tubules. Nanoplatelets with *c*-axes along the 90° azimuth tended to be located to the left and right of the tubule. Orientation of cAp *c*-axes tangential to the tubule axes confirmed the anticipated biaxial crystallographic texture (Stock *et al*., 2011). The map in Figure 2B covered a region between two tubules. The texture remained continuous in the intertubular region.

The average 00.2 cAp *d*-spacing in both the longitudinal and transverse direction was 3.441 ± 0.005 Å for all samples. The 00.2 *d*-spacings did not change significantly with location within any of the mapped areas. From the average longitudinal and transverse *d*-spacings, the average residual strains were 30 ± 700 με, a value essentially equal to zero.

The average FWHM of the 00.2 peak for all points in all the area maps was 7.8 ± 1.8 pixels (0.031 ± 0.007° 2θ). Assuming a nanoplatelet size of 50 nm along the *c*-axis direction (Deymier-Black *et al*., 2012), the average ε_{rms} was 8,500 ± 3,500 με. The FWHM and thus the ε_{rms} did not vary significantly with location within any one diffraction map or between different maps (data not shown).

Figure 4 compares vertical and horizontal line scans of 2.11+diffraction peak intensity across a single tubule with the corresponding Ca and Zn fluorescent intensity profiles. The scan positions are shown in the Ca fluorescence map (upper left). In both directions, all three profiles were in good agreement, that is, the intensities rose and fell together. There was a suggestion of higher Ca signal at the two of the lumen edges, consistent with weak hyper-

[3]Here and below, the values are mean ± 1 standard deviation.

calcification in early stage PTD, and these weak peaks corresponded to equally subtle local maxima in 211+ diffracted intensity. On both sides of each of the vertical and horizontal Zn profiles, small peaks were present.

XANES

Figure 5 plots Zn fluorescent intensity as a function of incident X-ray energy spanning the Zn K-edge. The edges of the zinc gluconate hydrate (Zn^{2+}) sample and dentin coincide while that of the Zn metal foil is displaced. This clearly demonstrates that the Zn in the dentin specimen is in the 2+ state and not metallic.

Discussion

Fluorescence and diffraction mapping of bovine ITD was successfully performed with a resolution of 200 nm. This is a 36% increase in spatial resolution from earlier work (Stock *et al*., 2011), that is, from a beam diameter of 250–200 nm, that significantly improves mapping. Improvements in shielding reduced background intensity and improved the quality of the fluorescence spectra and the diffraction patterns, making up for the decrease of sampled cAp nanoplatelets from ~5,000 (irradiated volume of 250 × 250 × 1,000 nm^3) to ~3,200 (200 × 200 × 1,000 nm^3).

Selection of Tubules

The tubules mapped here and in Stock *et al*. (2011) were not too tightly clustered; other areas of the sections had tightly clustered or sparsely distributed tubules, for example, Figure 2 of Stock *et al*. (2011). The characterized tubules, therefore, represent a “typical” structure. The spatial extremes may show differences from the “typical” tubules, but this requires data beyond the scope of this study.

Zn and Ca Distribution

The Ca fluorescence of these near-pulp samples showed little evidence of hyper-calcification at the edges of the tubule lumens. Since hyper-mineralization is the signature of PTD (Takuma and Eda, ’96; Weber, ’68; Weiner *et al*., ’99), this confirms that the samples are from a region of the tooth where PTD had only begun to develop. The fluorescence data indicated that Zn was elevated in the dentin near the tubules compared to the regions remote from the tubules in agreement with Stock *et al*. (2011). The results from the present study and from Stock *et al*. (2011) firmly establish that Zn is concentrated in the near-tubular dentin in root dentin of this tooth. The maps in Figure 2 also show that Zn is inhomogeneously distributed around the circumference of the tubule lumen; there is no relationship of Zn content with the orientation of the fluorescence detector. Inhomogeneous Zn distribution results in Zn profiles from line scans (Fig. 3) being higher than the circumferential average profiles from the area maps; the circumferential averages included areas with Zn concentrations near background.

The concentration of Zn remains to be determined. If one were to assume that the ratio of Zn and Ca fluorescent intensities represent the ratio of elemental compositions, the data suggests Zn amounts to 5–6% of Ca. This estimate ignores differences in fluorescent yield

for the two elements and very significant matrix absorption effects for the sample (measurements around holes in a plate) and for the experimental geometry, a subject worthy of a report in its own right.

Previous studies have shown that Zn is the most plentiful trace element in human dentin (Driessens and Verbeeck, ’90), and concentrations vary somewhat over the bulk of the dentin except near pulp region where the concentration is significantly elevated (Brudevold *et al*., ’63). In bone and cartilage, increased Zn concentrations have been found in regions of ongoing mineralization (Vincent, ’63; Zoeger *et al*., 2008). In bone, Gomez *et al*. (’99) found that Zn was present in three separate pools: free Zn associated with the surrounding fluids; Zn bound to cAp mineral; and Zn bound to organic molecules.

Because the dentin samples in the present study are cleaned and fully dehydrated, fluid associated Zn does not contribute to the Zn fluorescence signal. Studies on synthetic hydroxyapatite systems have shown that at high pH (pH 10) and elevated temperatures, Zn will substitute for Ca (Ren *et al*., 2009). These substitutions result in an increased P/Ca ratio and a decrease of the 00.2 *d*-spacing. Although substitution of Zn for Ca in cAp is unfavorable especially under physiological conditions (Tang *et al*., 2009), it is possible to have some Zn exchange. However, the maps of the P/Ca ratio in Figure 2 do not show an increase in the P/Ca co-localized with increases in Zn. The P/Ca ratio is lower immediately adjacent to the tubule lumen (Fig. 2), and the peak in Zn signal is farther away from the lumen. Secondly, the $d_{00.2}$ is relatively constant over the mapped areas and does not change where Zn fluorescence intensity peaks; its value of 3.441 ± 0.005 Å is consistent with reported values for hydroxyapatite containing 0–5% Zn (3.446 ± 0.002–3.4345 ± 0.003 Å) (Ren *et al*., 2009). This suggests that no more than 5% Zn could be incorporated in the dentin’s cAp, even at the positions of peak Zn fluorescent intensity. Finally, if Zn were continuously incorporated into the bulk of the cAp nanoplatelets, the peak in Zn content near the tubules would require a significant increase in the rate of Zn incorporation in those volumes.

An alternative consistent with the diffraction and fluorescence results is that the “excess” Zn is not substituted into the cAp lattice but is present in dentin’s organic constituents. The XANES data indicating Zn^{2+} is consistent with association with these organic components, but it also does not rule out substitution into the cAp lattice. It is not possible to identify the organic components using the techniques described here, but they could be phospholipids (observed near tubule lumens in bovine dentin (Gotliv and Veis, 2007)) or Zn containing metalloenzymes such as alkaline phosphatase (Gomez *et al*., ’99) or transcription factors such as Osterix. These metalloenzymes and Osterix are associated with biomineralization in dentin (Chen *et al*., 2009; Foster *et al*., 2012). The role of these Zn containing organic species indicate that the increase in Zn in the near-tubular dentin may indicate a mineralizing front for PTD or ITD.

Crystallographic Texture

Quantifiable diffraction patterns were produced, despite the decreased sampling volume, indicating that this technique effectively provides X-ray diffraction data from thin mineralized specimens at high resolution. Only diffraction peaks associated with cAp were

identified in the diffraction patterns, demonstrating that no other crystalline phases were present. Fitting these entire cAp diffraction rings (pseudo-Voigt curves) quantified integrated intensity, FWHM, and peak position as a function of position.

Maps of the azimuthal variation of 00.2 integrated intensity (i.e., intensity as a function of azimuthal angle and location, Fig. 2A,B) indicate that the cAp platelets' long axes (*c*-axis) lie tangential to the circumference of the tubules, confirming previous studies showing the collagen fibril axes are circumferentially aligned about the tubules and that the cAp *c*-axes parallel the fibril axes (Ten Cate, '80). This type of crystallographic texture is termed biaxial in materials science. Maps centered around single tubules show that texture is continuous from the tubules' edge to the intertubular regions suggesting that Zn content does not affect the texture. Maps covering the area between tubules show that the texture does not vary between neighboring tubules. This indicates that there is no sharp change in orientation between collagen deposited about one tubule as compared to its nearest neighbor, consistent with the standard picture of simultaneous, space-filling collagen deposition by adjacent odontoblasts (Ten Cate, '80) and with simple geometry (tangents to contacting disks, i.e., area associated with each odontoblast, are parallel at their point of contact). This is unlike osteonal bone where there is a clear change in orientation at the interface where two osteons meet or between lamellae within an osteon (Currey, 2002). A consequence of this texture may be toughening of dentin: a crack exiting the tubule radially, as would be expected for a hole in a plate, would be forced to break mineralized collagen fibrils lying across its path (whatever the direction of extension) or to change direction and become highly non-planar at the 100 nm level (Rasmussen and Patchin, '84; Nalla *et al*., 2003). Both of these processes consume energy, limiting the ability of the crack to propagate. Similarly, the lack of distinct interfaces between ITD associated with different adjacent tubules may be advantageous mechanically as a potential low-energy path for crack propagation does not exist.

Even highly oriented specimens will only approximate an ideal texture. There can be spreads of orientation, for example, and this is certainly seen in Figure 2. In some of the maps, however, the diffracted intensity for a given azimuth is significantly larger on one side of a tubule than the other, from example, higher at the 8 o'clock than the 2 o'clock positions in the 120° azimuthal map of Figure 2A. These observations might reflect nothing more than a difference in sample thickness, but the simultaneously recorded Ca fluorescent intensity map shows a weak but opposite variation in intensity. With thickness variation ruled out, that leaves orientation effects, that is, the plane of biaxial symmetry may be tilted relative to the plane of thin section, and hence to the orientations sampled by diffraction. In both the Ca and the total integrated intensity maps of Figure 2, the tubule lumens appear quite elongated. Only the nanoplatelets oriented to satisfy Bragg's law will contribute to the diffracted intensity, that is, those nanoplatelets whose *c*-axes are at the Bragg angle ($\theta =$ 10.2°) with respect to the incident beam direction (Warren, '90; Cullity and Stock, 2001). Therefore, if the field of view examined in Figure 2A contained one region where many nanoplatelets were tilted to satisfy Bragg's law and another region where few were correctly tilted, diffraction intensity from the later region would be lower than that from the former.

Strains

Millimeter-sized samples of bovine dentin contain an initial cAp pre-strain or residual strain of −1,000 to −2,250 με (Deymier-Black *et al*., 2010). These pre-strains in cAp, which are comparable to those in bone, may limit crack propagation and crack opening (Ascenzi and Benvenuti, ’77; Ascenzi, ’99). The residual strains in the present study equal zero, indicating that the residual strain in cAp has been released during sample preparation. The 1 μm thickness of the sample is only enough to contain 5–10 collagen fibrils (diameter ~100 to 200 nm (Orgel *et al*., 2011)). Without the bulk matrix to retain the in-grown stress, the cAp residual strains would be expected to relax.

The FWHM of the diffraction patterns did not vary significantly with position suggesting that neither size of the cAp crystals nor the strain distribution changes appreciably with distance from the tubules. Assuming a size of 50 nm, as determined from previous X-ray measurements on bovine dentin (Deymier-Black *et al*., 2010, 2012), the present study found ε_{RMS} = 8,500 ± 3,500 με. This is larger than previously measured values of 5,000–6,600 με for bovine dentin (Deymier-Black *et al*., 2010, 2012). Instrumental broadening corrections are not yet available for the 2-ID-D instrument; they are probably significant given the focusing geometry and diffraction angles and may account for the difference. Damage to near-surface cAp nanoplatelets from the microtome sectioning cannot be ruled out, and the depth to which such damage reaches may not be a negligible fraction of the total thickness. On the other hand, atomic force microscopy demonstrated that microtomed surfaces were smoother than polished bone surfaces (Xu *et al*., 2003).

Conclusion

Tubules in the PTD-free regions of bovine dentin were mapped using synchrotron X-ray diffraction and X-ray fluorescence at a resolution of 200 nm. This increased resolution allowed mapping of the variation of Ca, P, and Zn content as well as cAp nanoplatelet orientation at a scale that is approximately ten times smaller than the tubule size. X-ray fluorescence and XANES results indicated that the near tubule dentin contained high levels of Zn^{2+}. Diffraction results suggest that the Zn is likely not present in the mineral phase but in the organic phase, possibly as phospholipids, as transcription factors such as Osterix, or as metalloenzymes such as alkaline phosphatase. These Zn^{2+}-containing organic species play important roles in biomineralization and may indicate the presence of a mineralizing front for ITD or PTD. Improved analysis of the X-ray diffraction data allowed accurate measurement of the biaxial texture of the cAp about the tubules. This texture is continuous from the edge of the tubules to the remote ITD and even between tubules. This continuous orientation may play an important role in dentin mechanics as it serves as an efficient crack arrestor.

Future studies should include the use of X-ray standards to accurately convert raw counts into Zn concentrations. Further, chemical modification, such as the removal of lipids (Bligh and Dyer, ’59) could serve to identify the possible Zn hosts in dentin. Collection of both the cAp 00.2 and cAp 00.4 diffraction peaks would improve analysis of crystal size and ε_{RMS}.

The use of thicker samples would increase the number of diffractors and improve counting statistics while maintaining or even improving the throughput of samples; the cost would be degraded spatial resolution if the tubules were not precisely perpendicular to the sectioning plane. The data to date suggest that the Zn and cAp structural gradients are not extreme, at least at the 200 nm level, and such through-thickness averaging may not affect conclusions drawn from the maps. A further advantage of thicker samples is that the significant volume will be farther than 0.5 μm from a prepared surface, mitigating concerns about sample preparation artifacts.

Acknowledgments

Contract grant sponsor: NICDR; contract grant number: DE001374; contract grant sponsor: US Department of Energy, Office of Science, Office of Basic Energy Sciences; contract grant number: DE-AC02-06CH11357.

The authors thank Mr. Lennell Reynolds for preparing the microtome sections, Dr. A. Telser for help surveying the thin sections with optical microscopy and Dr. J.D. Almer (APS, Sector 1) for providing the diffraction analysis programs. A.V. received funding from NICDR (contract grant number: DE001374).

References

Almer JD, Stock SR. Internal strains and stresses measured in cortical bone via high-energy X-radiation. J Struct Biol. 2005; 152:14–27. [PubMed: 16183302]

Ascenzi A, Benvenuti A. Evidence of a state of initial stress in osteonic lamellae. J Biomech. 1977; 10:447–453. [PubMed: 893478]

Ascenzi M-G. A first estimation of prestress in so-called circularly fibered osteonic lamellae. J Biomech. 1999; 32:935–942. [PubMed: 10460130]

Bligh EG, Dyer WJ. A rapid method of total lipid extraction and purification. Can J Biochem Physiol. 1959; 37:911–917. [PubMed: 13671378]

Brudevold F, Steadman LT, Spinelli MA, Amdur BH, Gron P. A study of zinc in human teeth. Arch Oral Biol. 1963; 8:135–144. [PubMed: 14016161]

Chen S, Gluhak-Heinrich J, Wang YH, et al. Runx2, osx, and dspp in tooth development. J Dent Res. 2009; 88:904–909. [PubMed: 19783797]

Cullity, BD.; Stock, SR. Elements of X-ray diffraction. Upper Saddle River, NJ: Prentice Hall; 2001.

Currey, JD. Bones: structure and mechanics. Princeton, NJ: Princeton University Press; 2002.

Deymier-Black AC, Almer JD, Stock SR, Haeffner DR, Dunand DC. Synchrotron X-ray diffraction study of load partitioning during elastic deformation of bovine dentin. Acta Biomater. 2010; 6:2172–2180. [PubMed: 19925891]

Deymier-Black AC, Singhal A, Yuan F, Almer JD, Brinson LC, Dunand DC. Effect of high-energy X-ray irradiation on creep mechanisms in bone and dentin. J Mech Behav Biomed Mater. 2013; 21:17–31. [PubMed: 23454365]

Driessens, FCM.; Verbeeck, RMH. Biominerals. Boca Raton, FL: CRC Press; 1990.

Foster BL, Nagatomo KJ, Tso HW, et al. Tooth root dentin mineralization defects in a mouse model of hypophosphatasia. J Bone Miner Res. 2012; 28:271–282. [PubMed: 22991301]

Gomez S, Rizzo R, Pozzi-Mucelli M, Bonucci E, Vittur F. Zinc mapping in bone tissues by histochemistry and synchrotron radiation-induced X-ray emission: correlation with the distribution of alkaline phosphatase. Bone. 1999; 25:33–38. [PubMed: 10423019]

Gotliv B-A, Robach JS, Veis A. The composition and structure of bovine peritubular dentin: mapping by time of flight secondary ion mass spectroscopy. J Struct Biol. 2006; 156:320–333. [PubMed: 16600633]

Gotliv B-A, Veis A. Peritubular dentin, a vertebrate apatitic mineralized tissue without collagen: role of a phospholipid-proteolipid complex. Calcif Tiss Int. 2007; 81:191–205.

Hammersley, AP. ESRF98HA01T: ESRF Internal Report. 1998. FIT2D V9.129 reference manual V3.1.

Kinney JH, Balooch G, Marshall SJ, Marshall GW, Weihs TP. Hardness and young's modulus of human peritubular and intertubular dentine. Arch Oral Biol. 1996; 41:9–13. [PubMed: 8833584]

Libera J, Cai Z, Lai B, Xu S. Integration of a hard X-ray microprobe with a diffractometer for microdiffraction. Rev Sci Instrum. 2002; 73:1506–1508.

Nalla RK, Kinney JH, Ritchie RO. Effect of orientation on the in vitro fracture toughness of dentin: the role of toughening mechanisms. Biomater. 2003; 24:3955–3968.

Orgel J, Antipova O, Sagi I, et al. Collagen fibril surface displays a constellation of sites capable of promoting fibril assembly, stability, and hemostasis. Conn Tiss Res. 2011; 52:18–24.

Rasmussen ST, Patchin RE. Fracture properties of human enamel and dentin in an aqueous environment. J Dent Res. 1984; 63:1362–1368. [PubMed: 6595288]

Ren F, Xin R, Ge X, Leng Y. Characterization and structural analysis of zinc-substituted hydroxyapatites. Acta Biomater. 2009; 5:3141–3149. [PubMed: 19446055]

Singhal A, Deymier-Black AC, Almer JD, Dunand DC. Effect of high-energy X-ray doses on bone elastic properties and residual strains. J Mech Behav Biomed Mater. 2011; 4:1774–1786. [PubMed: 22098877]

Stock SR, Veis A, Telser A, Cai Z. Near tubule and intertubular bovine dentin mapped at the 250 nm level. J Struct Biol. 2011; 176:203–211. [PubMed: 21821132]

Takuma S, Eda S. Structure and development of the peritubular matrix in dentin. J Dent Res. 1996; 45:683–692.

Tang Y, Chappell HF, Dove MT, Reeder RJ, Lee YJ. Zinc incorporation into hydroxylapatite. Biomater. 2009; 30:2864–2872.

Ten Cate, AR. Oral histology: development, structure and function. St Louis: Mosby; 1980.

Vincent J. Microscopic aspects of mineral metabolism in bone tissue with special reference to calcium, lead and zinc. Clin Orthop Rel Res. 1963; 26:161–175.

Warren, BE. X-ray diffraction. Reading, MA: Addison-Wesley; 1990.

Weber DF. The distribution of peritubular matrix in human coronal dentin. J Morphol. 1968; 126:435–446. [PubMed: 5716436]

Weiner S, Veis A, Beniash E, et al. Peritubular dentin formation: crystal organization and the macromolecular constituents in human teeth. J Struct Biol. 1999; 126:27–41. [PubMed: 10329486]

Xu J, Rho JY, Mishra SR, Fan Z. Atomic force microscopy and nanoindentation characterization of human lamellar bone prepared by microtome sectioning and mechanical polishing technique. J Biomed Mat Res-A. 2003; 67A:719–726.

Zoeger N, Streli C, Wobrauschek P, et al. Determination of the elemental distribution in human joint bones by SR micro XRF. X-Ray Spectrom. 2008; 37:3–11.

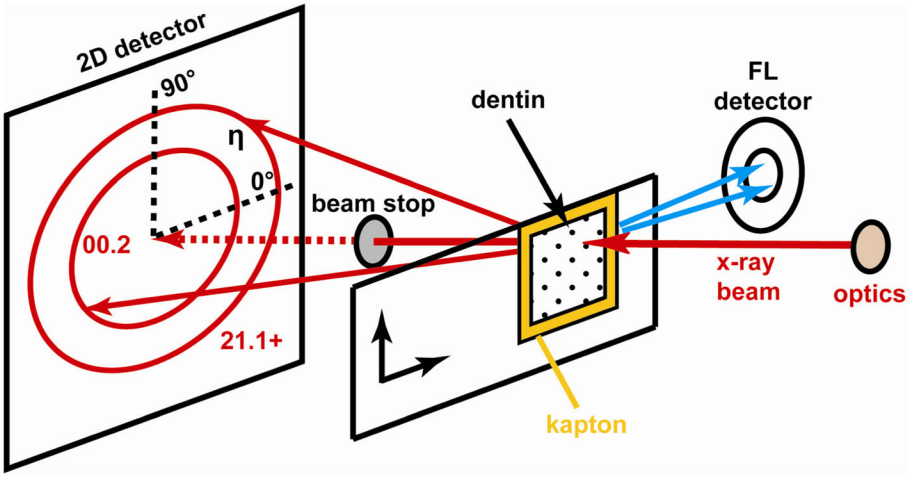

Fig 1.

Experimental set-up showing positions of the sample and fluorescence and diffraction detectors. The azimuthal angle η of the diffraction rings is also shown.

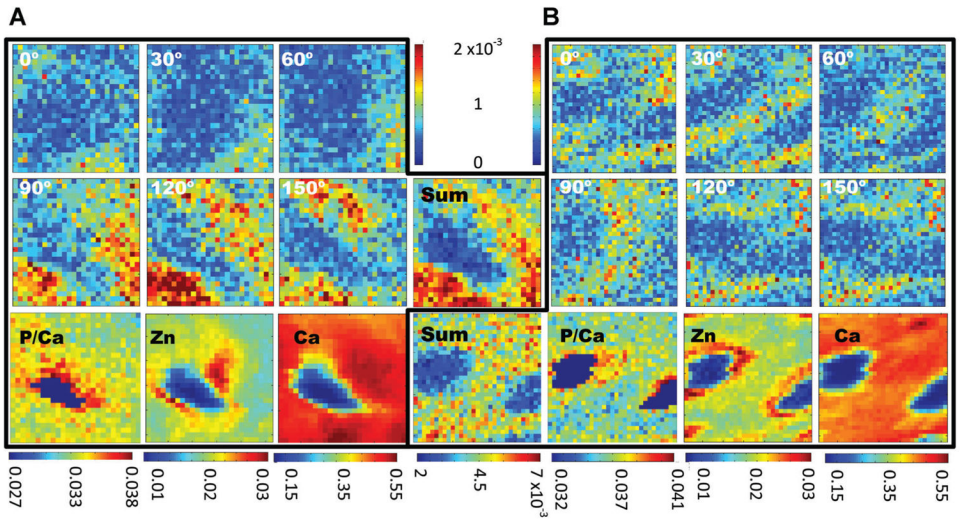

Fig 2.

Texture and fluorescence maps for two of the area scans covering 6 μm × 6 μm. The texture maps (top six maps in A and B) are plots of 00.2 diffraction intensity at the specified azimuthal orientation (±15°) as a function of position. The scale (shown in the top center) is the diffraction intensity normalized to the incident beam intensity, and maps of the total ("sum") of diffracted intensity appear in the center below the intensity color bars. The scale below the sum maps is the total diffraction intensity normalized to the incident beam intensity. The ratio of phosphorous-to-calcium fluorescence intensities is shown in the bottom left. The Zn and Ca fluorescence intensities are shown to the center and left of the bottom row. The scales, shown below the maps, are fluorescence intensities normalized to the incident beam intensity.

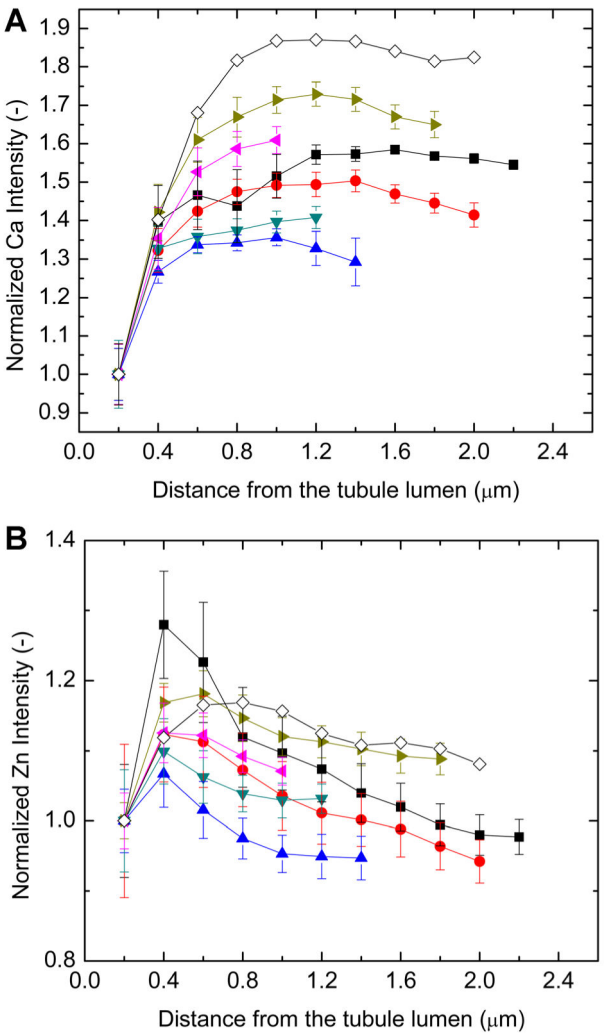

Fig 3.

Plots of Ca (A) and Zn (B) fluorescent intensities for the area mapsaround (circumferentially averaging around the tubule lumen) and for the line scans across tubules. The single plot with open diamonds represents the average profile of Zn and Ca intensity from the line scans; the other plots are from individual tubules and show circumferentially averaged intensities from the area maps. In both cases, the Ca fluorescence intensity increases from the tubule lumen edge and quickly reaches a plateau. The Zn intensity reaches a peak at ~0.4 μm from the lumen edge, decreases, and then plateaus ~1 μm from the lumen edge.

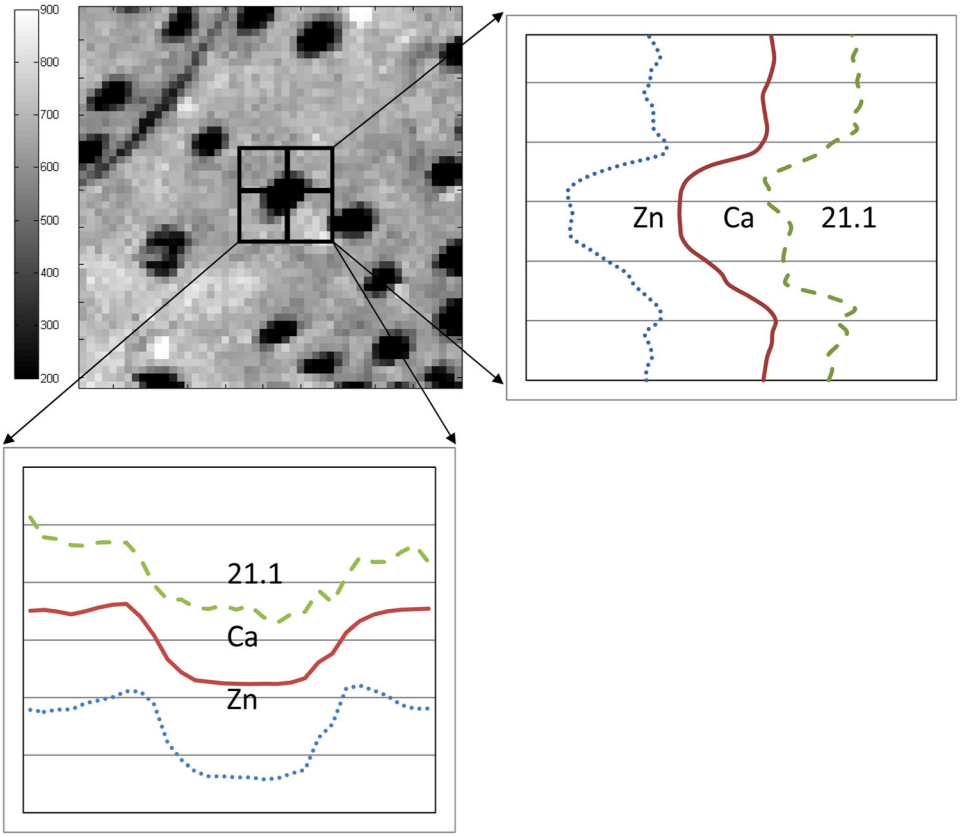

Fig 4.

Line scans showing the integrated intensity of the 21.1+ diffraction peak, Ca fluorescence intensity, and Zn fluorescence intensity across a single tubule. The specific tubule and its surroundings are shown in the 25 × 25 μm^2 Ca fluorescence map at the top left. Note that the fluorescence and diffraction intensity profiles correspond closely.

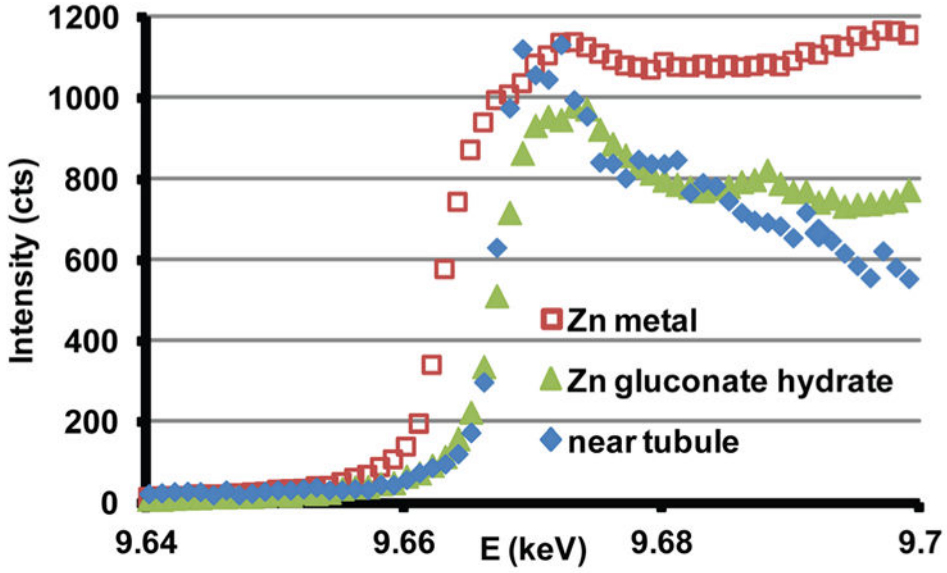

Fig 5.

XANES patterns spanning the Zn K-edge from a dentin thin section, zinc gluconate hydrate powder (Zn^{2+}) and zinc metal foil.